Inversion strategy based on joint QND assessments

Marko Scholze

Hans Chen

Thomas Kaminski

Michael Vossbeck

che-project.eu

Co-ordinated by ECMWF

D3.6 Inversion strategy based on joint QND assessments

Dissemination Level:	Public
Author(s):	Marko Scholze, Hans Chen (Lund University) Thomas Kaminski, Michael Vossbeck (The Inversion Lab)
Date:	26/10/2020
Version:	1.0
Contractual Delivery Date:	30/092020
Work Package:	3
Document Owner:	ULUND
Contributors:	ULUND, iLab
Status:	Final

CHE: CO2 Human Emissions Project

Coordination and Support Action (CSA)
H2020-EO-3-2017 Preparation for a European capacity to monitor CO2 anthropogenic emissions

Project Coordinator: Dr Gianpaolo Balsamo (ECMWF)
Project Start Date: 01/10/2017
Project Duration: 39 months

Published by the CHE Consortium

Contact:
ECMWF, Shinfield Park, Reading, RG2 9AX,
gianpaolo.balsamo@ecmwf.int

The CHE project has received funding from the European Union's Horizon 2020 research and innovation programme under grant agreement No 776186.

Table of Contents

Figures

Tables

1 Executive Summary

This document reports on the work and the results obtained in task 3.5 'Perform QND experiments with an advanced data assimilation system (CCFFDAS) to establish inversion strategy'. It provides a description of the CCFFDAS modelling framework, the applied QND methodology as well as the results obtained from the work performed in task 3.5 'Perform QND experiments with an advanced data assimilation system (CCFFDAS) to establish inversion strategy'. We have developed a prototype of a global Carbon Cycle Fossil Fuel Data Assimilation System (CCFFDAS) that combines the functionalities of the Fossil Fuel Data Assimilation System by Asefi-Najafabady et al. (2014) and of the Carbon Cycle Data Assimilation System by Kaminski et al. (2017a). The CCFFDAS was applied to assess a number of design aspects of the upcoming Monitoring and Verification Support capacity as part of the Copernicus CO_2 Monitoring mission (CO2M). The assessment was based on the Quantitative Network Design technique and quantified the mission's performance in terms of the posterior uncertainty in the totals of the sectorial fossil CO_2 emission rates for selected countries and the first week in June 2008. The emissions were classified into two sectors, one for electricity generation and the other for all other emissions denoted as the "other" sector. We analysed two different observing networks, ground based in situ observations and satellite based total column observations, in a range of configurations.

We find that

- At country scale, a single CO2M satellite achieves posterior uncertainties in the weekly sectorial emission rates well below the weekly emission rate for the national total for the sectors, assuming that annual emissions are evenly divided between all weeks.
- For each sector, a constellation of four satellites achieves a larger reduction in posterior uncertainty, i.e. the number of satellites matters. This added value of the extra satellites is more pronounced for the other sector than the electricity generation sector, where the uncertainty over China is reduced by about 30% for this particular case (first week in June 2008) when going from a single satellite to the four-satellite constellation. This is below the theoretical possible 50% reduction due to the different satellite tracks and with it differences in cloud cover and systematic errors for this particular week.
- Correlated systematic errors in the satellite XCO2 can seriously degrade the performance, resulting in increased posterior uncertainties from 15% to almost 130% relative to the case with no systematic errors.
- The representation error due to the mismatch in resolution between the satellite images and the atmospheric transport model increases posterior uncertainties, however, these uncertainties will be decreased when the resolution of the transport model is increased.
- If national inventories at weekly time scale were available, their inclusion would result in a strong reduction in posterior uncertainty (the largest reduction we obtained from all our experiments) compared with using atmospheric observations only, which quantifies the synergy / complementarity between the atmospheric (and other) observations and the inventories. The synergistic exploitation of diverse data steams is a particular strength of the CCFFDAS approach. However, by including national inventory data in the assimilation the obtained results are not an independent estimation of the emissions from atmospheric data anymore.
- A hypothetical projection of the posterior uncertainties in the weekly emission rate to the annual scale shows the potential for a CCFFDAS / CO2M verification mode (operating independently from the inventories), which may provide useful information that is complementary to the inventories with uncertainty ranges in the same order of magnitude.
- The inclusion of surface observations does not result in substantial uncertainty reductions for sectorial emissions compared with the default experiment with one

satellite. However, we note that the current in situ network was not designed for observing anthropogenic emissions, nevertheless it is important to observe background conditions and validate satellite measurements.
- Adding radiocarbon observations helps to further constrain emission rates from the other sector especially for countries with a larger proportion of biogenic fluxes such as e.g. Brazil and Poland.

2 Introduction

2.1 Background

The CO_2 Human Emissions (CHE) project has been tasked by the European Commission to prepare the development of a European capacity to monitor anthropogenic CO_2 emissions. The monitoring of fossil fuel CO_2 emissions has to come with a sufficiently low uncertainty in order to be useful for policymakers. In this context, the main approaches to estimate fossil fuel emissions, apart from bottom-up inventories, are based on inverse transport modelling either on its own or within a coupled carbon cycle fossil fuel data assimilation system. Both approaches make use of atmospheric CO_2 and potentially other tracers (e.g., radiocarbon, co-emitted species such as CO and NOx) and either rely on the availability of prior fossil fuel CO_2 emission estimates and uncertainties (for inverse transport modelling), or are able to make use of such information as an additional constraint (in the carbon cycle fossil fuel data assimilation system). Inverse transport modelling also requires prior biogenic flux estimates and uncertainties.

WP3 evaluates the current status of uncertainty quantification in fossil fuel emissions through bottom-up inventories as well as inverse modelling and data assimilation. For the latter top-down methods, possible improvements in uncertainty reduction from enhanced space-borne and in situ observation scenarios for fossil CO_2 emissions are quantified based on observing system simulation experiments (OSSEs) and quantitative network design (QND) studies using different approaches: a) high resolution inverse transport modelling of CO_2 and co-emitted species and b) advanced carbon cycle-fossil fuel data assimilation system (CCFFDAS) integrating atmospheric, terrestrial and socioeconomic datasets.

This deliverable provides a description of the CCFFDAS modelling framework, the applied QND methodology as well as the results obtained in task 3.5 ‘Perform QND experiments with an advanced data assimilation system (CCFFDAS) to establish inversion strategy’.

2.2 Scope of this deliverable

2.2.1 Objectives of this deliverable

The main objectives of this deliverable are to

- document the development of the quantitative network design framework around coupled models of the terrestrial and anthropogenic carbon fluxes,
- describe the observations and the corresponding observation operators,
- provide a set of network design experiments, and
- present results of the network design experiments regarding the options for designing a prototype MVS capacity.

2.2.2 Work performed in this deliverable

After consultation with the partners involved within task T3.5, a summary of the work within T3.5 and the corresponding results has been compiled.

2.2.3 Deviations and counter measures

Not applicable.

3 Framework overview

The CCFFDAS modelling framework is shown in Figure 1 highlighting the flow of information from the control vector (yellow oval, consisting of model process parameters and initial conditions in atmospheric CO_2) to the observations (here denoted as blue ovals).

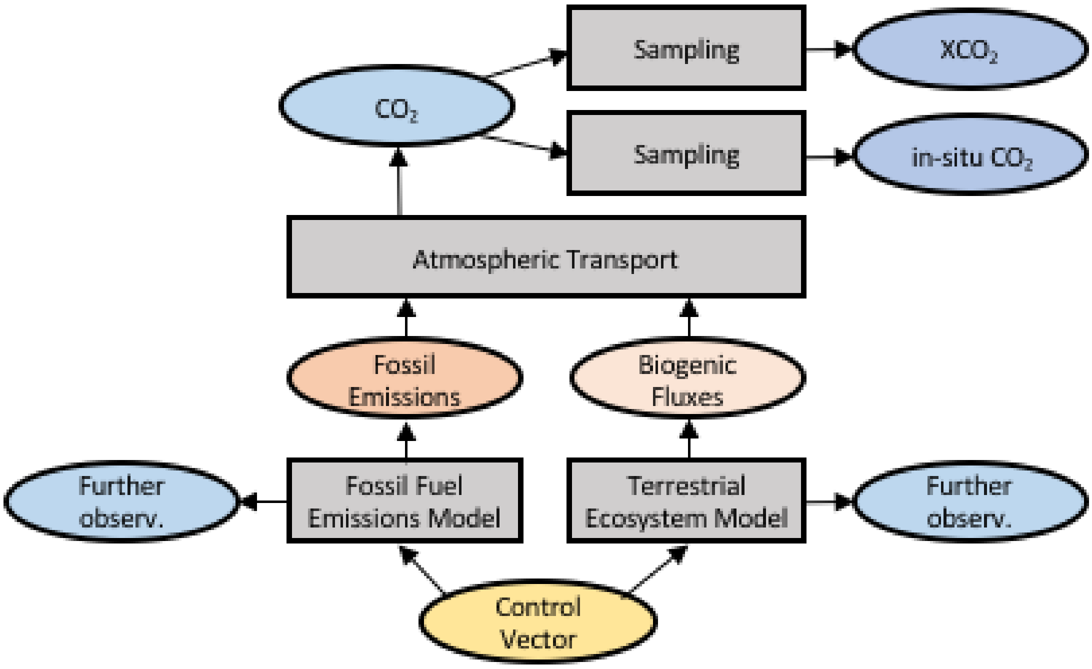

Figure 1: Modelling framework with information flow in CCFFDAS. Boxes represent calculation steps by models, blue ovals observables, yellow oval the control vector (model parameters and initial condition), and red ovals surface fluxes (fossil emissions, terrestrial fluxes).

Task 3.5 ‘Perform QND experiments with an advanced data assimilation system (CCFFDAS) to establish inversion strategy’ co-developed and applied a prototype carbon cycle-fossil fuel data assimilation system that combines the functionalities of the Fossil Fuel Data Assimilation System by Asefi-Najafabady et al. (2014) and the Carbon Cycle Data Assimilation System by Kaminski et al. (2017a). Substantial development work of the CCFFDAS employed here has been co-funded by the European Space Agency funded CCFFDAS (ESA-CCFFDAS) project. While the emphasis in the ESA-CCFFDAS project was on the different design options of the CO2M satellite, here the focus is on assessing the impact of different observation networks (in situ and satellite) and combinations thereof on the performance in terms of the posterior uncertainty quantification for the selected target quantities. The selected target quantities are the national emission totals per sector (i.e., for power generation and the ‘other’ sector, see Section 5.1) for the first week of June 2008 and for five countries: Australia, Brazil, China, Germany, and Poland.

In the following sections we provide a short summary description of the Quantitative Network Design (QND) approach employed in this study (Section 4) as well as an overview of the individual models (Section 5.1 for the fossil fuel emissions model component and Section 5.2 for the natural terrestrial CO_2 fluxes model component). Detailed descriptions of the observations and observation operators are given in Section 6.

4 Quantitative Network Design Approach

The QND formalism employed here is presented in detail by Kaminski and Rayner (2017); it is partly based on Tarantola (2005) and Rayner et al. (2016). We provide only a shortened form of the presentation by Kaminski and Rayner (2017a).

QND performs a rigorous uncertainty propagation from the observations to a target quantity of interest relying on the indirect link from the observations to the target variables established by a numerical model. We distinguish between four sources of uncertainty in a model simulation:

1. Uncertainty caused by the formulation of individual process representations and their numerical implementation (structural uncertainty).
2. Uncertainty in constants / process parameters in the formulation of these processes (parametric uncertainty).
3. Uncertainty in external forcing/boundary values, such as temperature or precipitation, driving the relevant processes (boundary value uncertainty).
4. Uncertainty in the state of the system at the beginning of the simulation (initial state uncertainty).

The first category reflects the implementation of the relevant processes in the model (code) while the others can be represented by a set of input quantities controlling the behaviour of a simulation using the given model implementation. The underlying assumption is that these different uncertainties are uncorrelated. The QND procedure formalises the selection of these input quantities through the definition of a control vector, x. The choice of the control vector is a subjective element in the QND procedure. A good choice covers all input quantities with high uncertainty and high impact on simulated equivalents of observations d_{mod} or target quantities y (Kaminski et al., 2012; Rayner et al., 2016).

A target quantity may be any quantity that can be extracted from a simulation with the underlying model, but also any component of the control vector. In the general case, where the target quantity is not part of the control vector, the QND procedure operates in two steps. The first step (inversion step) uses the observational information to reduce the uncertainty in the control vector, i.e. from a prior to a posterior state of information. The second step (prognostic step) propagates the posterior uncertainty forward to the simulated target quantity.

Within the QND formalism, we represent all involved quantities by probability density functions (PDFs). We typically assume a Gaussian form for the prior control vector and the observations, if necessary after a suitable transformation. The covariance matrices of the Gaussian PDFs express the uncertainty in the respective quantities, i.e. $C(x_0)$ and $C(d_{\mathrm{obs}})$ for the prior control vector and the observations, respectively. In the context of these PDFs we will use the term uncertainty to refer to its full covariance matrix in the case of a vector quantity, and in the case of a scalar quantity or a given vector component it refers to the square root of the entry on the diagonal of the full covariance matrix corresponding to that particular vector component. In the latter case the uncertainty refers to one standard deviation of the marginal PDF corresponding to that component, and we use the notation $\sigma(d_2)$ to denote, for example, the standard deviation of the second component of d.

For the first QND step we use a mapping M from control variables onto equivalents of the observations. In our notation the observation operators that map the model state onto the individual data streams (see Kaminski and Mathieu (2017) and Section Observations and observation operators6) are incorporated in M. M is in practise computed by a specific numerical model with specific inputs and outputs. Let us first consider the case of a linear model, for which we denote by $\mathbf{M}'$ the Jacobian matrix of M, i.e. the derivative of M with respect to x. In this case, the posterior control vector is described by a Gaussian PDF with uncertainty $C(x)$, which is given by

$$\boldsymbol{C}(x)^{-1} = \mathbf{M'}^T \mathbf{C}(d)^{-1} \mathbf{M'} + \boldsymbol{C}(x_0)^{-1}, \tag{1}$$

where the data uncertainty $C(d)$ is the combination of two contributions:

$$C(d) = C(d_{\text{obs}}) + C(d_{\text{mod}}). \tag{2}$$

The term $C(d_{\text{obs}})$ expresses the uncertainty in the observations and $C(d_{\text{mod}})$ the uncertainty in the simulated equivalents of the observations $M(x)$. The first term in Equation (1) expresses the impact of the observations and the second term the impact of the prior information. In the non-linear case we use Equation (1) as an approximation of $C(x)$.

The mapping N involved in the second step is the mapping from the control vector onto a target quantity, y. The Jacobian matrix $\mathbf{N}'$ of the mapping N is employed to approximate the propagation of the posterior uncertainty in the control vector $C(x)$ forward to the uncertainty in a target quantity, $\sigma(y)$ via

$$\sigma(y)^2 = \mathbf{N}' C(x) \mathbf{N'}^T + \sigma(y_{\text{mod}})^2. \tag{3}$$

If the model were perfect, $\sigma(y_{\text{mod}})$ would be zero. In contrast, if the control variables were perfectly known, the first term on the right-hand side would be zero. The terms $C(d_{\text{mod}})$ in Equation (2) and $\sigma(y_{\text{mod}})$ in Equation (3) capture the structural uncertainty as well as the uncertainty in those process parameters, boundary and initial values that are not included in the control vector. These two terms typically rely on subjective estimates. When comparing the effect of different data sets in the same setup, $\sigma(y_{\text{mod}})$ acts as an offset (for the respective variance) in Equation (3). As the focus in the present study is on an assessment of data products rather than on the performance of the components in our modelling chain, we ignore $\sigma(y_{\text{mod}})$.

To conduct a valuable QND assessment, the requirement on the model is not that it simulates the target quantities and observations under investigation realistically, but rather that it provides a realistic *sensitivity* of the target quantities and observations under investigation with respect to a change in the control vector. (As a hypothetical example we can think of a perfect regional tracer model that is run with an offset in the initial or boundary conditions for a passive tracer. The simulated tracer concentration will carry this offset, but all sensitivities will be perfect.)

We note that (through Equation (1) and Equation (3)) the posterior target uncertainty solely depends on the prior and data uncertainties, the contribution of the model error to the uncertainty in the simulated target variable, $\sigma(y_{\text{mod}})$, as well as the observational and target Jacobians (quantifying the linearised model responses of the simulated observation equivalent and of the target quantities). Hence, the QND formalism can be employed to evaluate hypothetical candidate networks. Candidate networks are characterised by observational data type, location, sampling frequency and time, and data uncertainty but not the observational value. Here, we define a network as the complete set of the characterisation of observations, d, used to constrain the model. The term network is not meant to imply that the observations are of the same type or that their sampling is coordinated. For example, a network can combine different types of in situ and satellite observations. In fact, one of our assessments deals exactly with this case: It combines XCO2 observed from space with in situ observations of atmospheric CO_2, while all our other assessments evaluate either XCO2 or in situ observations.

Our inverse problem is characterised by a high-dimensional control vector combined with an observation vector of even larger dimension. As a consequence, the size of $\mathbf{M}'$ is too large to solve Equation (1) on powerful desktop computers. Hence, as Rödenbeck (2005), we restrict ourselves to computing posterior uncertainties for a number of selected target quantities. For a given target quantity with target Jacobian $\mathbf{N}'$ we iteratively solve Equation (4) for the target z:

$$\mathbf{N}'^T = C(x)^{-1} z \,. \tag{4}$$

Combining this with Equation (3) yields:

$$\sigma(y)^2 = \mathbf{N}' z \;. \tag{5}$$

The Jacobians are computed by automatic differentiation of the model code with the software tool TAPENADE (Hascoët and Pascual, 2013). The observational Jacobian $\mathbf{M}'$ is of the dimension of the control vector times the dimension of the set of all observations, which varies from experiment to experiment. Both dimensions are high. For example in the case of a single CO2M satellite with only nadir view observations together with nightlights and sectorial national totals the dimension of the observation vector is above 1.6 million. The dimension of the control vector is about 1.6 million, mainly due to the gridcell-dependent parameters for the other sector emissions on the high-resolution 0.1 degree grid. The matrix $\mathbf{M}'$ thus has more than 10^{12} entries. To enhance the numerical efficiency we exploit the sparsity of $\mathbf{M}'$, and restrict the calculation of $\mathbf{M}'$ to non-zero elements. In particular we exploit that fact that the submatrix relating the per capita gross domestic product (GDP) to the nightlights (both of dimension of about 1.5 million) has a diagonal structure.

5 Description of individual models

5.1 Description of the fossil fuel emissions model

The underlying model for the fossil fuel CO_2 emissions is based on Asefi-Najafabady et al. (2014) using a sectorial approach. We define two sectors here: a power generation sector and all other emissions denoted as the “other” sector. Following the Kaya identity (Nakicenovic, 2004) the emissions F from the other sector at a point x in country c are given by

$$F(x,c) = pP(x)g(x)ef(c) \tag{6}$$

where p is a scalar multiplier for the population density, P is the population density, g is the per capita GDP, e is the energy intensity of the economy and f is the fossil carbon intensity of energy. Here, lower case variables denote elements of the control vector (see Table 1). In summary, these are a scalar multiplier for the population density (p), a pointwise estimate of the per capita GDP ($g(x)$), a global constant for the energy intensity of the economy (e), and a country-wise estimate for the carbon intensity of energy production ($f(c)$). For the carbon intensity we apply an uncertainty of 10 times its prior value (denoted as f_0 in Table 1) with a floor value of 10^{-6} kgC/MJ. $P(x)$ is the population density. The population dataset we use is the gridded population density provided by the LandScan Global Population Database (available at www.geospatial.com). The data set represents population density at 0.00833 × 0.00833 degrees grid resolution for the year 2008 (Bhaduri et al., 2007). The population density is then aggregated to the 0.1 degree resolution used here.

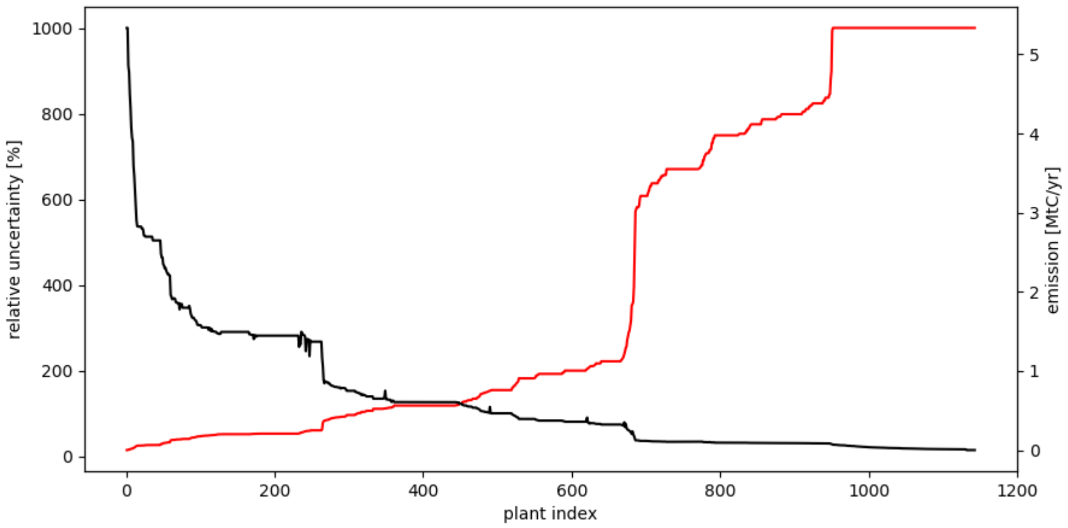

Figure 2: Emission rates (black) and their relative uncertainty (red) for the power plants in China. Relative uncertainties above 1000% are show as 1000%.

For the power generation sector we use the emissions from a list of power plants in each country. As in Asefi-Najafabady et al. (2014) emissions associated with each power plant were mapped onto the FFDAS grid based on the power plant location. If power plants were located inside a grid cell, the grid cell was given the emission value with no subgrid cell spatial distribution. When location information was not available for a power plant, the power plant emissions were proportionally distributed to the rest of the grid cells containing power plants in that country. Control variables in the power generation sector are the emissions from each listed power station (see Table 1). These emissions are obtained from the so-called CARMA database (see http://carma.org). Uncertainties on these power plant emissions are estimated from the average of the reported standard error from plants listed in the US Energy Information

Administration and/or the US EPA Clean Air Market datasets. For a detailed description of the emission and emission uncertainty estimates from the world's power plants we refer to the supporting material of Asefi-Najafabady et al. (2014).

We use a floor value of 0.01 MtC for the prior uncertainty of an individual power plant to ensure that smaller power plants, which may have large relative emission uncertainties, are accounted for in the optimization. This results in relative prior uncertainties well above 100% for small power plants. As an example, Figure 2 shows emission rates and their relative uncertainty for the power plants in China. Using this procedure, the prior uncertainties aggregated to country-scale were below our assumed uncertainty for the International Energy Agency (IEA) national totals (IEA, 2011) for four countries (China, India, South-Africa, and USA). In contrast to Asefi-Najafabady et al. (2014), in each of these four countries the prior uncertainty for each of the power plants was upscaled such as to match the uncertainty in the national total.

Table 1: List of control variables for the fossil fuel emissions model.

Description	Symbol	Resolution	Prior Uncertainty
Per capita GDP	*g*	gridcell	1,25 dollar/yr/person
Energy intensity	*e*	global	10^{-6} MJ/dollar
Carbon intensity	*f*	country	max($10f_0$, 10^{-6} kgC/MJ)
Population density scaling	*p*	global	10^{-6}
Nightlight scaling	*n*	global	see Equation (11)
Power plant emissions (CARMA)	*u*	individual power plants	see Section 5.1

For both the power generation and the other sector, prior values of the control variables in this study are selected such that they are consistent with the IEA and the nightlights observations. The corresponding sectorial fluxes for Europe are shown in Figure 3.

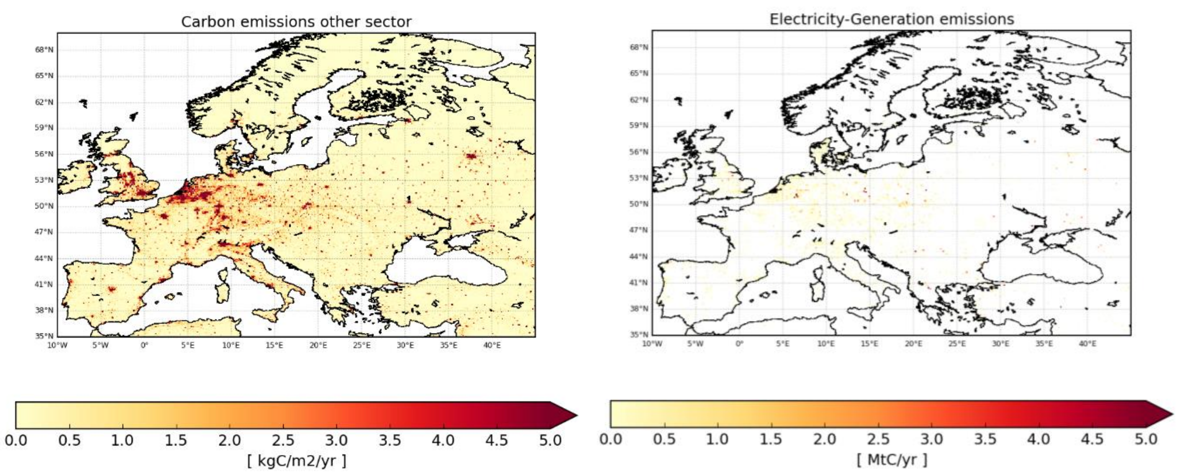

Figure 3: Fossil fuel emissions for 2008 as calculated by FFDAS for the 'other' (left panel) and the electricity generation sector (right panel).

5.2 Description of the terrestrial biosphere carbon flux model

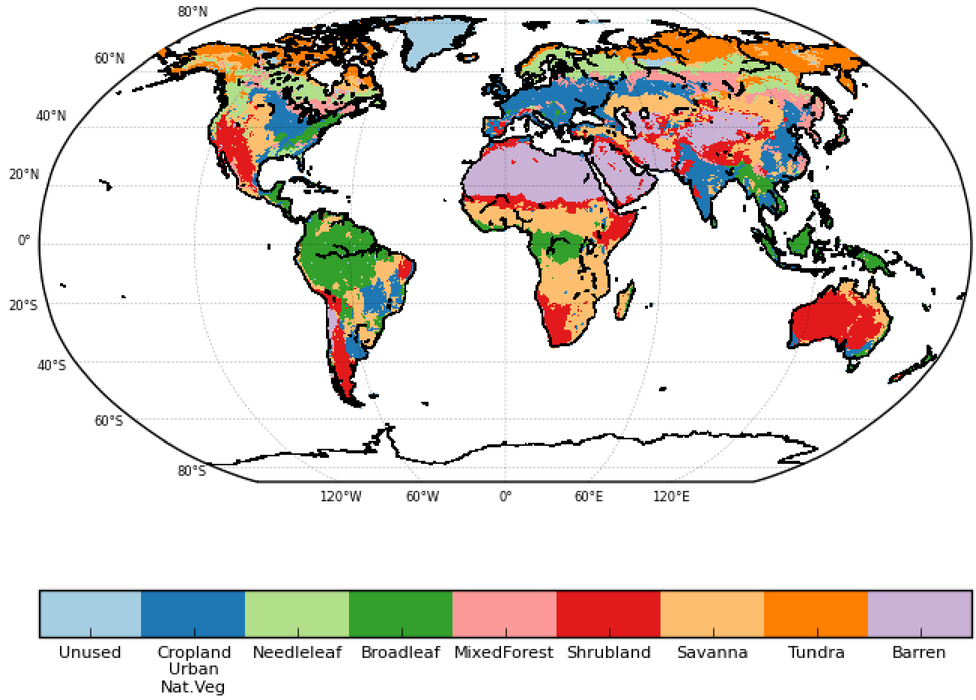

Figure 4: Plant functional type groupings by land cover classes: cropland/urban/natural vegetation mosaic, needle-leaf forest, broadleaf forest, mixed forest, shrubland, savanna, tundra, and barren/sparsely vegetated.

The terrestrial biosphere model we used to calculate the natural terrestrial CO_2 exchange fluxes is conceptionally similar to the one used by Kaminski et al. (2002) and based on Knorr and Heimann (1995). The model was previously employed for assimilation of XCO2 (Kaminski et al., 2017a). It operates on a 0.5 degree global grid and divides the global terrestrial biosphere into 8 land cover classes (in the following also referred to as Plant Functional Types, PFTs) based on the MODIS land cover classification (Friedl et al., 2010), see Figure 4:

- cropland/urban/natural vegetation mosaic,
- needleleaf forest,
- broadleaf forest,
- mixed forest,
- shrubland,
- savanna or grassland,
- tundra,
- barren or sparsely vegetated.

The model calculates the uptake of CO_2 by photosynthesis (expressed as Net Primary Productivity, NPP) using the so-called light-use efficiency approach:

$$\mathrm{NPP}(x,t) = \epsilon \cdot \alpha(x,t) \cdot \mathrm{FAPAR}(x,t) \cdot \mathrm{srad}(x,t) \qquad (7)$$

where ϵ denotes the PFT-specific parameter for light use efficiency, α a water stress factor, FAPAR the fraction of absorbed photosynthetically active radiation, and srad the incident solar radiation driving photosynthesis.

Heterotrophic respiration $\mathrm{R_{het}}$ is calculated following a Q_{10} functional relationship with temperature T and is, as the photosynthesis calculation, modulated by the water stress factor:

$$\mathrm{R_{het}}(x,t) = n(x) \cdot \alpha(x,t) \cdot Q_{10}^{T/10} \tag{8}$$

The PFT-specific parameter Q_{10} expresses the ratio of respiration at T + 10 to that at T, with T measured in °C. The control variables for the terrestrial biosphere model component are the parameters ϵ and Q_{10} (see Table 2). The spatially varying normalisation factor $n(x)$ is the ratio of the temporal integrals of $\mathrm{NPP}(x,t)$ and $\mathrm{R_{het}}(x,t)$ computed for prior parameter values over the entire model simulation period from 2004 to 2008. The normalisation factor thus ensures a balanced prior biosphere over the model simulation period but allows for non-zero posterior net flux. This is different from the study by Kaminski et al. (2002) which assimilated the observed seasonal cycle and enforced an annually balanced posterior biosphere.

In summary, the model uses as driving data global fields of temperature, FAPAR, and the water stress factor. The temperature fields are taken from the CRU data set (Harris et al., 2014) and the plant water-stress factor, taken as monthly climatological AET/PET (actual divided by potential evapotranspiration) values per grid-cell, is computed with the BETHY model of Knorr (2000) for the years 1989 to 2012 using the same CRU data set to provide meteorological input data for BETHY. We use the FAPAR product (Pinty et al., 2011) derived with JRC-TIP (Pinty et al., 2007) directly on the 0.5 degree model grid, to avoid significant errors which would be imposed by spatial aggregation of the FAPAR product derived on a finer grid; for details we refer to Kaminski et al. (2017b).

Table 2: List of control variables for the terrestrial biosphere fluxes model.

Description	Symbol	Resolution	Prior Uncertainty
Light use efficiency	ε	PFT	100% of prior
Respiration relation to temperature	Q_{10}	PFT	100% of prior

The values for the prior model parameters (ϵ and Q_{10}) have been selected such that they are consistent with XCO2 observations obtained from GOSAT (Kaminski et al., 2017a).

6 Observations and observation operators

The observation operator needed in data assimilation translates model state information to observational variables. In the following subsections we describe the observations and the corresponding observation operators in our CCFFDAS modelling framework.

6.1 IEA national totals

On an annual scale, national total fossil fuel CO_2 emissions are key observations for constraining the simulated fossil fuel emissions. The data are provided by IEA (IEA, 2011). IEA estimates CO_2 emissions from fossil fuel combustion using energy surveys for 137 individual countries and 3 country aggregates (a collection of smaller countries in Asia, Africa, and Latin America).

In addition to national totals, the IEA emissions are divided into (sub-)sectors. For our purposes here, we aggregate the sectorial emissions into two sectors according to our fossil fuel emissions model: The first sector is the power generation sector and includes all power-producing facilities including both grid-connected and 'autoproducers' facilities (generation of electricity for internal use not connected to the grid). We call the second sector the 'other' sector, which encompasses all other emitting categories (including industrial, residential, commercial, and transportation emissions).

IEA does not, unfortunately, supply any uncertainties on the emission estimates. In contrast to Asefi-Najafabady et al. (2014) we use the following approach to provide a transparent assignment of national total emissions uncertainties based on Marland (2008): We group the world's countries according to the United Nations Framework Convention on Climate Change (UNFCCC) Classification of Parties (countries) by the Annex, i.e. Annex I, Annex II and Non-Annex I countries (UNFCCC, 1992). We consider Annex II countries as countries with 'well-developed energy statistics and inventories' and assign these countries an uncertainty of 5% of the total emissions (at the 95% confidence level). For the purpose of assigning national total emissions uncertainty we consider Turkey, Monaco, and Liechtenstein as Annex II countries. Annex I countries that do not belong to the Annex II classification are classified as industrialised (developed) countries and assigned an uncertainty of 10% of the total emissions (at the 95% confidence level). All other countries, i.e. Non-Annex I countries, are assigned an uncertainty of 20% of the total emissions (at the 95% confidence level). Figure 5 shows a map of the country classification. The percentage values above are divided by 2 to represent a 1 sigma relative uncertainty of the sum over both sectors. To distribute the total uncertainty between the two sectors, we first compute the fraction of each sector's emissions of the total emission, and then compute the sectorial uncertainty by multiplying the square root of that fraction with the total uncertainty. This procedure ensures that the computed variances (i.e. squares of standard deviation) for both sectors add up to the total variance.

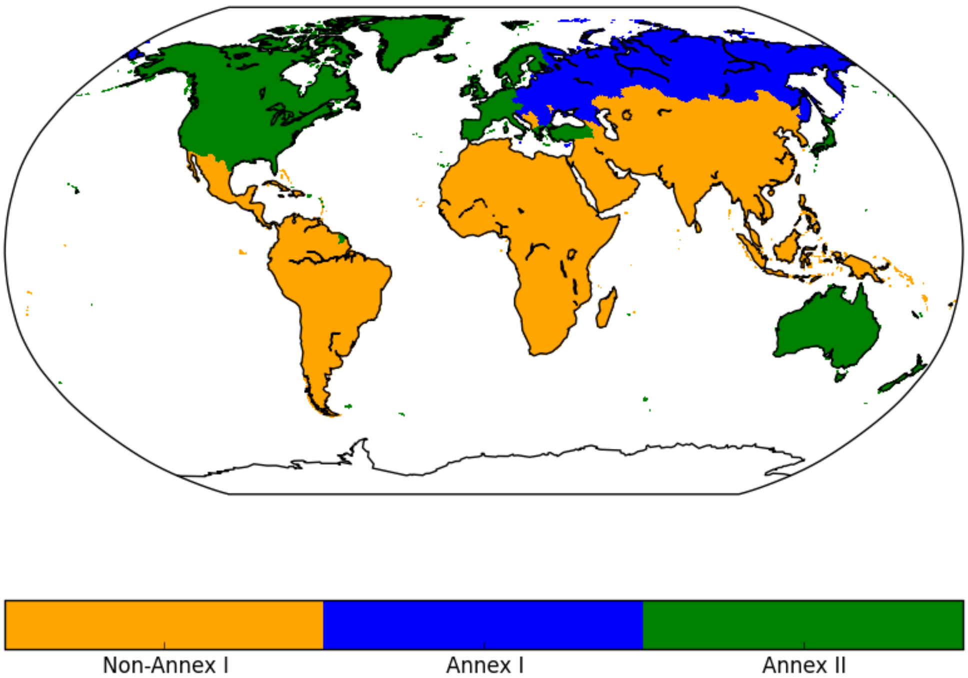

Figure 5: World map showing the UNFCCC country classification. Note that for the purpose of assigning national total emissions uncertainty we consider Turkey, Monaco, and Liechtenstein as Annex II countries and display them as such.

There are two observation operators associated with the IEA national emissions observations, one for each of the two sectors. We first describe the observation operator for the power generation sector and then the operator for the other sector.

Since the control variables for the power generation sector are the individual power plant emissions $u(i)$ (see Section 5.1 above) with index i representing an individual power plant and the observations are national total emissions for power generation $U(c)$ in a given country c, the power plant contribution to the observation operator is the sum of the emissions generated by the power plants located in the country c:

$$O_{\mathrm{elec}} = \sum_{i \in c} u(i). \tag{9}$$

The observation operator for the other sector is essentially the Kaya identity (Nakicenovic, 2004) relating fossil fuel CO_2 emissions to population density P, per capita GDP g, energy intensity of the economy e and the fossil carbon intensity of energy f. Here, population density P, per capita GDP g and carbon intensity of energy f are spatially explicit variables, whereas $P(x)$ and $g(x)$ are gridcell-dependent and $f(c)$ is country-dependent. x denotes a 0.1 by 0.1 degrees gridcell and c a country. e is assumed to be a global constant. Because the IEA observations for the other sector are also national totals, the observation operator is the aggregated sum of the Kaya identity for the country c:

$$O_{\mathrm{other}} = \sum_{x \in c} A(x) p P(x) g(x) e f(c) \tag{10}$$

where $A(x)$ is the area of gridcell x and p a scalar multiplier for the population density. The parameters p, $g(x)$, e and $f(c)$ are all control variables to be constrained by observations.

6.2 Nightlights

We use nightlights as an additional observation to constrain the fossil fuel emissions model. The Defense Meteorological Satellite Program (DMSP) operates the Operational Linescan System (OLS) that records low-light imaging data at night worldwide. The data are archived by the US National Oceanic and Atmospheric Administration at the National Geophysical Data Center (NGDC) (http://ngdc.noaa.gov/eog/index.html). At NGDC a set of procedures were developed to obtain a stable intercalibrated nightlights product covering several years (Ziskin et al., 2010). A total of six products were produced for the years 1997, 1999, 2000, 2003, 2004, 2006, and 2010. Using this product, we applied a linear interpolation to obtain nighttime lights for 2008.

Uncertainties in the nightlight observations arise from errors in the instrument as well as from aggregating the native 30" observation to the 0.1 degree grid used here. To estimate these uncertainties we use the same approach as in Asefi-Najafabady et al. (2014), given by

$$\sigma_{\mathrm{NL}} = (0.5 + 0.1x_{\mathrm{NL}})1.25 \tag{11}$$

where x_{NL} is the observed nightlight value. The uncertainty is inflated by 25% (the factor 1.25 in Equation (11)) to take errors in the temporal interpolation into account.

The observation operator for nightlights relates the product of per capita GDP $g(x)$, population density $P(x)$ and its scaling factor p to the nightlight observation by multiplying it with a normalisation factor n, which also accounts for the conversion of units from GDP to nightlight digital number:

$$O_{\mathrm{NL}} = npP(x)g(x). \tag{12}$$

n is a global constant and part of the control vector, i.e. we solve for it in the optimisation (as is done for p as mentioned above).

6.3 Atmospheric CO_2

6.3.1 CO2M

The study makes use of error data files that characterise the uncertainty of a hypothetical L3 product from the CO_2 Monitoring mission (CO2M) with 0.5 degree spatial and daily temporal resolution. These were produced by the IUP, University of Bremen within the ESA-CCFFDAS project. In brief, the L3e data files have been generated from corresponding “Level 2 error files” (L2e files) and corresponding Error Parameterization (EP) formulas (EPFs). The theoretical background is described by Buchwitz et al. (2013). The L2e files contain detailed information for each individual satellite footprint (ground pixel) such as time and location and all parameters needed to compute random and systematic XCO2 retrieval errors such as solar zenith angle, surface albedo, cirrus optical depth, etc., via the EPFs. The L2e files were generated for a single sounding precision of 0.7 ppm.

The conversion of the L2e files into L3e files has been done by “gridding”, i.e., (typically) by averaging the relevant values of all the individual footprints (of a given satellite) contained in a 0.5 degree grid cell for a given day.

Here we make use of two scenarios: a scenario with one satellite and a scenario with a constellation of four satellites flying in the same orbit but shifted in time.

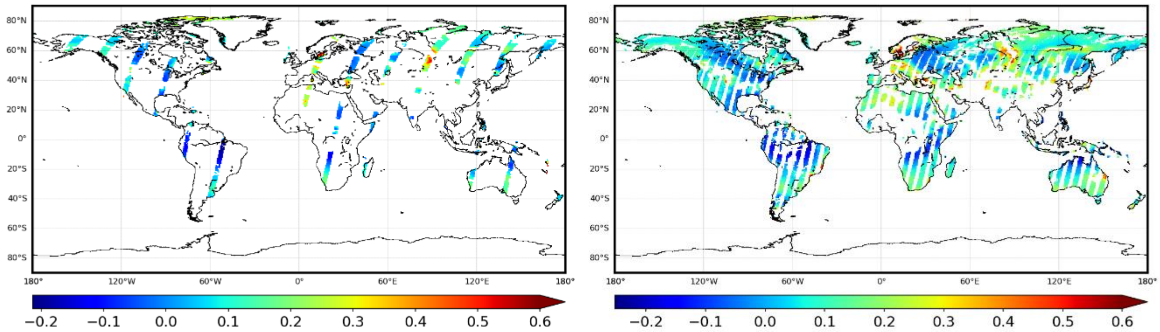

Figure 6: Spatial coverage for one day (1st of June 2008) of one (left) and four (right) hypothetical CO2M satellites (quality flagged, swath 250 km). The quantity shown is the XCO2 systematic error corresponding to each grid cell in ppm.

Note that “orbit” is the near-circular path of the satellites in space and because of the Earth rotation during the movement of the satellites this implies that different airmasses are observed by a constellation of four satellites. As a consequence, daily coverage is improved as the additional satellites fill the gap between the one satellite orbit, see Figure 6. All the above data files were produced for a swath width of 250 km.

Each data file provides observational uncertainty data sets for satellite ground pixels over land with corresponding errors computed with the “nadir EPF”.

The observation operator for the XCO2 atmospheric column observations used in this study is the global atmospheric transport model TM3 (Heimann and Körner, 2003), operated on its fine grid, i.e. with approximately 4 by 5 degrees horizontal resolution on 19 vertical levels. The model is approximated by a Jacobian that resolves monthly flux impacts in the same month as the observation and up to three months before an observation on the full model grid. Monthly flux impacts between four and 47 months before an observation are assumed to be uniform within a set of twelve latitudinal bands, each about 16 degree wide. For fluxes more than 47 months before an observation, we use a globally uniform response. This approximation is described in detail by Kaminski et al. (2010), with the exception that here we use 12 latitude bands instead of 8. The model is run for the years 2004 to 2008 (the year that our L3e files are representing) with meteorological driving fields taken from the NCEP reanalysis (Kalnay et al., 1996). The column-averaged CO_2 were sampled from the model to correspond to the daily XCO2 observation equivalent of CO2M in our assimilation framework.

For the QND experiments the uncertainty of the atmospheric XCO2 provided by the hypothetical L3 product must be aggregated to the 4 by 5 degrees horizontal resolution of the observation operator. We explore three different ways of aggregation. Throughout all experiments the random error at the native 0.5 degree resolution is treated as uncorrelated in space and time. In the default experimental setup, we do the same for the systematic error (Equation (13)).

$$\sigma_{\mathrm{tm}^2} = \left(\frac{1}{n}\right)^2 \sum RE_{0.5}^2 + \left(\frac{1}{n}\right)^2 \sum SE_{0.5}^2 \qquad (13)$$

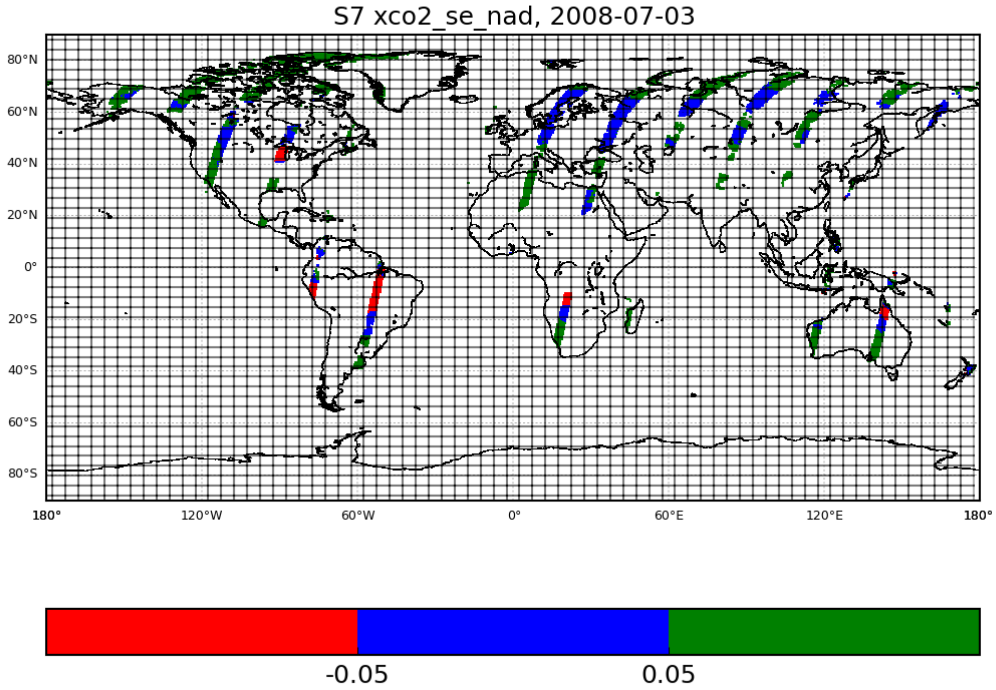

Figure 7: Ranges of systematic error of nadir view observed XCO2 from the hypothetical L3 product provided on a 0.5 degree grid. TM3 grid-cells with a resolution of around 4-by-5 degrees are illustrated by gridlines.

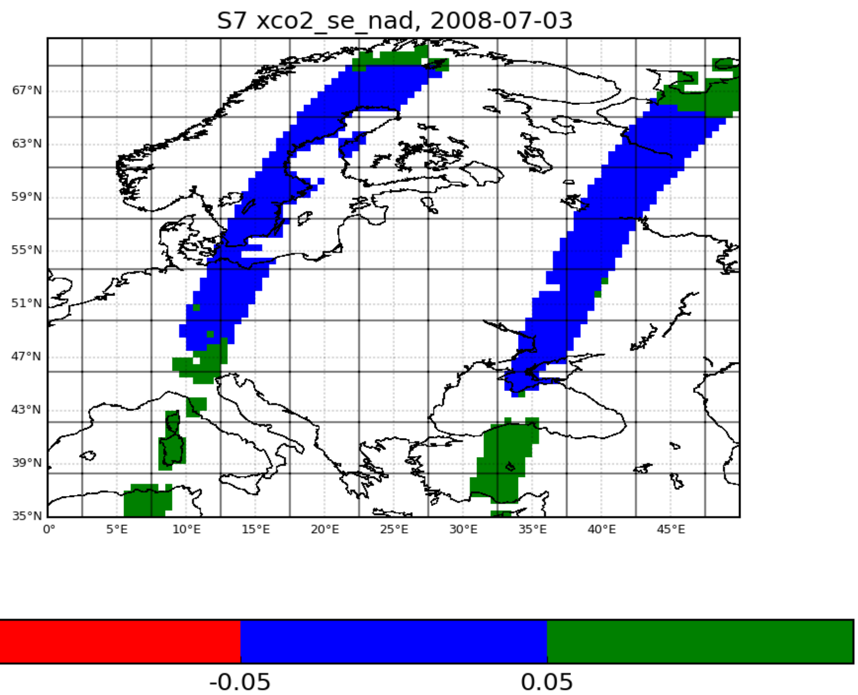

Figure 8: Ranges of systematic error of nadir view observed XCO2 from the hypothetical L3 product provided on a 0.5 degree grid focused over Europe. TM3 grid-cells with a resolution of around 4-by-5 degrees are illustrated by gridlines.

As an alternative aggregation procedure, Equation (14) shows the formalism when the systematic error is assumed to be correlated:

$$\sigma_{\mathrm{tm}^2} = \left(\frac{1}{n}\right)^2 \sum RE_{0.5}^2 + \left(\frac{n_{eps}}{n}\right)^2 \sum SE_{0.5,\mathrm{eps}}^2 + \left(\frac{n_+}{n}\right)^2 \overline{\mathrm{SE}_{0.5,+}}^2 + \left(\frac{n_-}{n}\right)^2 \overline{\mathrm{SE}_{0.5,-}}^2 \quad (14)$$

For this purpose we divide the systematic uncertainty into three independent subsets. The first subset is composed of all 0.5 degree grid cells with systematic uncertainty in the interval (-0.05 ppm, 0.05 ppm). The second (third) subset is composed of all 0.5 degree grid cells with systematic uncertainty above 0.05 ppm (below -0.05 ppm). The numbers of 0.5 grid cells in these three subsets are respectively denoted by n_{eps}, n_+, n_-, and the total number of grid cells as n. An illustration of the global distribution of the three groups is provided by Figure 7, and a zoom over Europe in Figure 8. In Equation (14) we assume that the systematic uncertainty within the first subset is uncorrelated, while we assume complete correlation within each of the other two subsets.

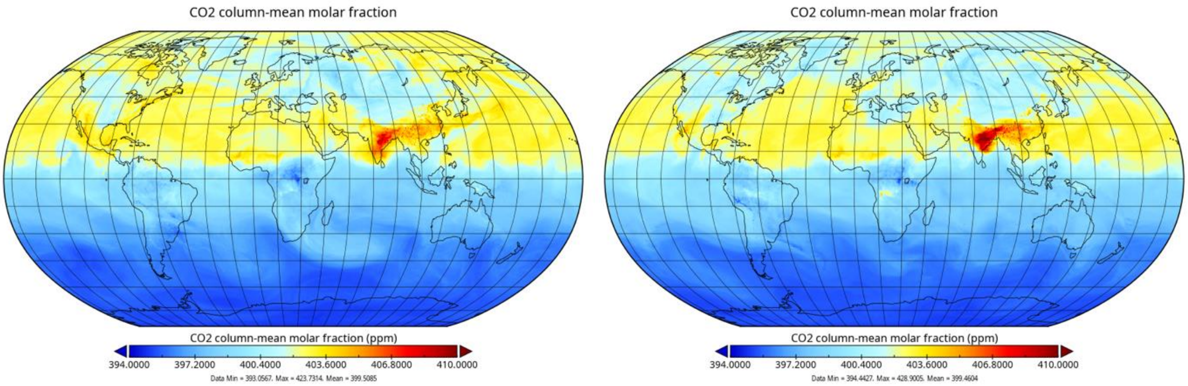

Figure 9: Daily mean of XCO2 simulated by ECMWF model for two days (left: 1st June; right: 7th June) in 2015 .

In an extreme case the aggregation into a TM grid cell may be based on only one single 0.5 degree grid cell. The aggregated product may then not represent the average over the TM grid cell particularly well. To approximate the uncertainty imposed by such representation errors, we use a third version for aggregation, which is based on Eq. 15 of Kaminski et al. (2010):

$$\sigma_{\mathrm{tm}^2} = \left(\frac{1}{n}\right)^2 \sum RE_{0.5}^2 + \left(\frac{1}{n}\right)^2 \sum SE_{0.5}^2 + \frac{1}{n} \sum \sigma_{\mathrm{het}}^2 \quad (15)$$

σ_{het} quantifies the heterogeneity, which we approximate as follows. We used a high-resolution simulation by the ECMWF model (Agustí-Panareda et al., 2019) and aggregated its daily mean XCO2 output (Figure 9) to the 0.5 degree grid of our XCO2 data. Within any given TM grid cell, σ_{het} was then computed as the variance in XCO2 over all covered 0.5 degree grid cells. Illustrations of the XCO2 uncertainties aggregated to the TM grid for a particular day in the first week of June and the three described aggregation methods are given in Figure 10.

For our assessments of multi-satellite configurations, we first apply the aggregation procedure for each satellite separately and use the resulting data sets as separate constraints. Similarly, we treat retrievals over land and ocean as separate constraints.

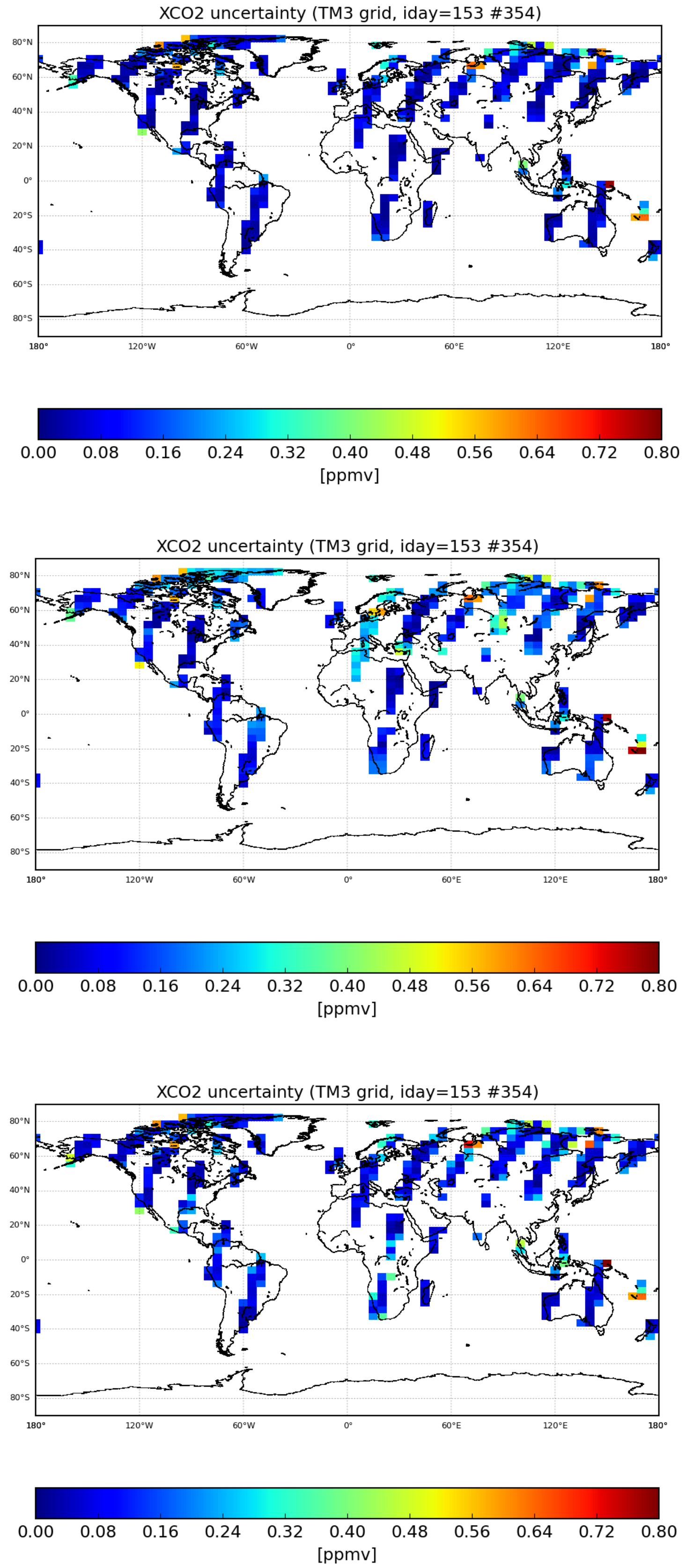

Figure 10: Overall uncertainty of nadir view observed atmospheric XCO2 for June 1st 2008 aggregated to TM grid by applying the aggregation formula from Equation (13) (top), Equation (14) (middle), and Equation (15) (bottom).

6.3.2 In situ CO_2

In our experiments, we compare the impact of XCO2 data with that of networks of in situ observations of atmospheric CO_2 (15 and 141 sites, see Figure 11). The 15-sites network samples essentially background air with the sites being located in remote areas. The larger 141-sites network represents the NOAA greenhouse gas flask sampling network (https://www.esrl.noaa.gov/gmd/ccgg/flask.php). We assume the network is equipped with continuous analysers, such that a daily mean value is available without any gaps. Throughout the network we use an uncertainty of 1 ppm for the daily means, reflecting the combined uncertainties in the observations and the model. We regard this as an optimistic choice: While the uncertainty for an hourly observation is typically assumed in the order of 0.3 ppm (Rödenbeck, 2005), our capability to simulate point measurements is limited. As an indication Table 3 provides the variability of hourly observations, which shows a maximum value of over 12 ppm for the Hegyhatsal tower (HUN) in Hungary.

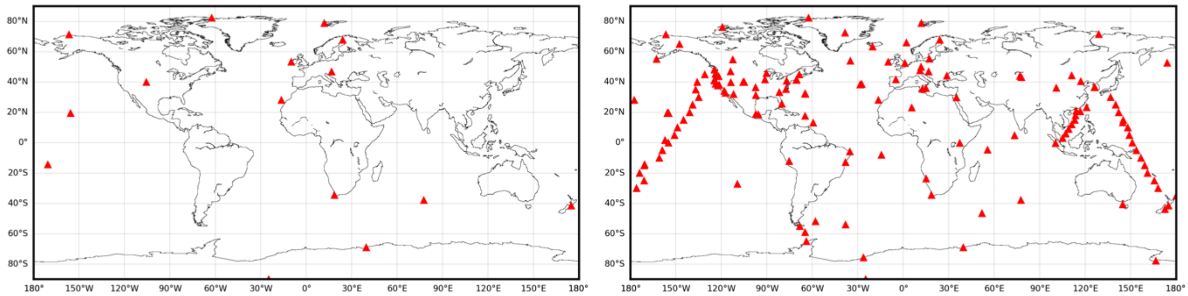

Figure 11: 15-sites (left) and 141-sites (right) network providing daily in situ observations.

The observation operator for the continuous network is identical to the one for XCO2 described in the previous section, except for the fact that here we sample the daily mean at the grid cell and vertical model transport layer in which the respective site is located, rather than computing a column average.

Table 3: Average, minimum, and maximum of daily standard deviation computed from observed hourly CO_2 concentrations (in ppm) for the first week in June for eight sites.

Site	Latitude	Longitude	mean	min	max
Alert, Canada	82.45 N	62.15 W	0.22	0.06	0.31
Amsterdam Island, Indian Ocean	37.8 S	77.54 E	0.26	0.12	0.44
Baring Head, New Zealand	41.41 S	174.87 E	1.64	0.68	2.89
Hegyhatsal, Hungary	46.95 N	16.65 E	10.64	7.55	12.9
Izana, Tenerife	28.31 N	16.5 W	0.63	0.37	1.01
Mace Head, Ireland	53.33 N	9.9 W	0.38	0.31	0.54
Mauna Loa, Hawaii	19.54 N	155.58 W	0.32	0.11	0.55
Pallas, Finland	67.97 N	24.12 E	1.08	0.47	2.28

6.3.3 Radiocarbon

Finally, we include experiments showing the potential constraints from in situ networks measuring radiocarbon ($^{14}CO_2$). For simplicity we assume here that radiocarbon is a perfect tracer of fossil fuel combustion-derived CO_2 with no uncertainties from e.g. nuclear power plant emissions or isotope disequilibrium fluxes from soils and the oceans. Moreover, we assume that the radiocarbon observations are co-located with the in situ CO_2 measurements to compare these different observations. The experiment considers an ideal scenario where continuous radiocarbon observations are available daily with an uncertainty of 1 ppm in fossil fuel CO_2, which is equivalent to about 2 permille uncertainty in $\Delta^{14}CO_2$.

The observation operator for radiocarbon is identical to the one for in situ CO_2 except that the radiocarbon observations do not have any sensitivity to the biogenic fluxes.

7 Experiments

Table 4: List of experiments; $ffCO_2$ = fossil fuel CO_2; EG = electricity generation sector.

Exp #	Observations	Error	Comment
0	-	-	Prior
1	1 satellite	0.7 ppm	Default, nadir view, uncorrelated systematic error
2	1 satellite	0.7 ppm	Nadir view, correlated systematic error
3	1 satellite	0.7 ppm	Nadir view, uncorrelated systematic error, including representation error
4	1 satellite	0.7 ppm	Nadir view, uncorrelated systematic error, 10 times larger prior error for EG
5	1 satellite	0.7 ppm	Nadir view, uncorrelated systematic error, including national totals as observations
6	4 satellites	0.7 ppm	Nadir view, uncorrelated systematic error
7	1 satellite + in situ 15 sites	0.7 ppm, 1 ppm	Nadir view, uncorrelated systematic error
8	In situ 15 sites	1 ppm	
9	In situ 15 sites	0.5 ppm	
10	In situ 15 sites with radiocarbon	1 ppm for CO2 and $ffCO_2$ (radiocarbon)	
11	In situ 141 sites	1 ppm	
12	In situ 141 sites with radiocarbon	1 ppm for CO2 and $ffCO_2$ (radiocarbon)	

Table 4 provides an overview on the experiments that we conducted. Experiments 1–6 constitute experiments assessing the impact of satellite observations only, while experiments 8–12 constitute experiments assessing the impact of in situ observations (both CO_2 and $^{14}CO_2$) only, and experiment 7 assesses the impact of satellite and in situ observations in combination.

Our experimental setup is such that we have defined a default experiment through the choice of several factors and based on this default then defined a number of further experiments, in each of which (with a few exceptions) only one of these impact factors is changed.

Regarding the XCO2 observations, our default configuration (Experiment 1 in Table 4) uses data for the first week of June provided by

- one satellite,
- with 250 km swath width,
- and the nadir view XCO2 data set based on retrievals over land,
- and on a single sounding accuracy of 0.7 ppm (see Section 6.3.1),
- which is aggregated to the model grid assuming spatially and temporally uncorrelated systematic errors, and
- ignores representation errors.

Experiment 2 explores the effect of correlations in the systematic errors of the XCO2 retrievals. Clearly, the representation error depends on the resolution of our transport model. To minimise this model-specific impact on our default experiment, we have by default not included it in the experiments but explore the effect of representation error in a specific sensitivity experiment (Experiment 3). Experiment 4 explores the effect of increasing the prior uncertainty for the energy sector by a factor of 10 with respect to the default experiment. The FFDAS of Asefi-Najafabady et al. (2014) has an annual time step, i.e. the system is operated with a fixed temporal emission profile at each grid cell and for each power plant. In order to relax this assumption, our default experiment restricts the temporal domain (assimilation window) to one week (the first week of June 2008), i.e. we are using atmospheric observations over that week to constrain the emission rates over that week. As the national inventories (Section 6.1) are only available on annual scale, the default experiment excludes them from the list of observations to be used to constrain the control vector. Experiment 5 addresses the hypothetical case of availability of national total emission rates on the weekly scale. Since the weekly emission rate uncertainties are not known, we assume the same emission rate uncertainty as on the annual scale applies. Experiment 6 increases the number of satellites to 4. Experiment 7 combines XCO2 with in situ CO_2 observations provided by the 15-sites atmospheric network (see Section 6.3.2), while Experiment 8 evaluates the 15-sites in situ CO_2 observations alone with our default uncertainty of 1 ppm. To test the impact of the observational in situ uncertainty we perform an experiment with the 15-site network but a reduced 0.5 ppm uncertainty (Experiment 9). Experiment 11 increase the size of the in situ network to 141 sites and Experiments 10 and 12 include radiocarbon measurements at the in situ sites of the two respective networks.

8 Results

We focus on the posterior uncertainties in national total emission rates during the first week of June 2008 for the two fossil fuel emissions sectors and five target countries. Tables 5 and 6 show the uncertainties in national emission rates for all experiments (see Section 7 and Table 4) for the electricity generation and ‘other’ sector, respectively. As a comparison, the first rows of the tables also list the national total emission rates (not uncertainty) for each target during this time period, assuming that the annual emissions are evenly distributed throughout the year. The second rows show the prior uncertainties before assimilating observations. Note that the prior uncertainties for the other sector are roughly ten times the national emission rates due to the specification of the prior uncertainty in the carbon intensity parameter (see Table 1: List of control variables for the fossil fuel emissions model.).

Table 5: Posterior uncertainty in emission rates (MtC/yr) for the electricity generation sector during the first week of June 2008. The first row (*National total*) shows actual emission rates (MtC/yr) instead of posterior uncertainties. EG = electricity generation sector.

Exp #	Description	Australia	Brazil	China	Germany	Poland
-	*National total*	60.0	11.2	855.2	92.0	43.2
0	Prior	14.7	9.1	123.5	22.6	11.9
1	Default, 1 satellite	14.1	9.0	115.7	22.6	11.9
2	1 satellite, correlated systematic error	14.5	9.0	119.9	22.6	11.9
3	1 satellite, representation error	14.4	9.1	119.3	22.6	11.9
4	1 satellite, inflated prior for EG	114.6	82.7	221.4	220.5	114.3
5	1 satellite + national totals	2.0	3.1	74.9	3.4	2.7
6	4 satellites	13.4	8.9	108.0	22.5	11.9
7	1 satellite + in situ 15 sites	14.1	9.0	115.7	22.6	11.9
8	In situ 15 sites	14.7	9.1	123.5	22.6	11.9
9	In situ 15 sites, 0.5 ppm uncertainty	14.7	9.1	123.5	22.6	11.9
10	In situ 15 sites with radiocarbon	14.7	9.1	123.5	22.6	11.9
11	In situ 141 sites	14.7	9.1	123.3	22.6	11.9
12	In situ 141 sites with radiocarbon	14.7	9.1	123.3	22.6	11.9

The uncertainty reductions in emission rates from the electricity generation sector are generally small. In the optimistic experiment with 4 satellites (experiment 6), the emission rate uncertainties are reduced relative to the prior uncertainty by 12.6% for China, 8.8% for Australia, 2.2% for Brazil, and less than 1% for Germany and Poland. The surface in situ network has a negligible impact on the emission rate uncertainties. These small uncertainty reductions could be due to high confidence in the prior compared with other components of the modelling chain, which would leave little room for optimisation for the electricity generation sector, or be due to low sensitivity of the observational networks to the emissions from the electricity generation sector. To test for the first possibility, we inflated the prior uncertainties for the electricity generation sector by a factor of ten to make them comparable to the prior uncertainties for the other section (**Error! Reference source not found.**), and then ran the QND experiment again using the default experiment with one satellite (experiment 1). Keeping in mind that the prior uncertainties are ten times larger than the default prior values in the second row of **Error! Reference source not found.**, the relative uncertainty reductions relative to the prior for the electricity generation emission rates with one satellite are now 82.1% for China, 22.0% for Australia, 9.1% for Brazil, 3.9% for Poland, and 2.4% for Germany.

Thus, in the case of large prior uncertainty of the emissions from the electricity generation sector, the satellite observations are able to provide useful constraints (smaller uncertainties than the national total emissions) on weekly national emissions for countries with large power plants like China.

Table 6: Posterior uncertainty in emission rates (MtC/yr) for the other sector during the first week of June 2008. The first row (National total) shows actual emission rates (MtC/yr) instead of posterior uncertainties. EG = electricity generation sector.

Exp #	Description	Australia	Brazil	China	Germany	Poland
-	*National total*	47.2	87.3	927.2	127.2	38.1
0	Prior	472.3	873.1	9272.0	1271.7	381.0
1	Default, 1 satellite	15.7	21.8	179.6	50.6	19.7
2	1 satellite, correlated systematic error	36.0	25.1	248.5	97.0	23.2
3	1 satellite, representation error	18.5	35.7	244.8	71.0	32.2
4	1 satellite, inflated prior for EG	102.2	89.9	286.7	280.7	138.6
5	1 satellite + national totals	1.8	8.3	96.0	4.0	2.7
6	4 satellites	13.2	15.1	124.5	41.2	17.2
7	1 satellite + in situ 15 sites	15.7	21.8	179.6	49.7	19.5
8	In situ 15 sites	472.3	873.1	9270.9	636.8	245.5
9	In situ 15 sites, 0.5 ppm uncertainty	472.2	873.1	9268.6	558.2	223.3
10	In situ 15 sites with radiocarbon	472.2	873.1	9268.6	584.4	212.2
11	In situ 141 sites	357.5	619.4	562.1	196.4	163.3
12	In situ 141 sites with radiocarbon	299.0	457.5	475.3	156.7	121.0

If information about the weekly emission rates was available independently form our emissions data base, for example collected from bottom-up inventories of national totals, this information could be treated as an additional data stream and assimilated into CCFFDAS. Experiment 5 illustrates such a case where both satellite observations and independent information about the national total emissions from the electricity generation sector are used to constrain emission rates, using the same prior uncertainties as the default experiment without inflation. In this case, there are substantial uncertainty reductions relative to the prior in the electricity generation sector across all target countries: 86.4% for Australia, 85.0% for Germany, 77.3% for Poland, 65.9% for Brazil, and 39.4% for China. The uncertainty reductions in Brazil and China are smaller compared with the other target countries because their assumed uncertainties in IEA national totals are larger (see Section **Error! Reference source not found.**). These results show that if independent information about emissions are available at weekly time scale, it is possible to combine this bottom-up information with top-down constraints from atmospheric measurements in the CCFFDAS approach to achieve a strong reduction in posterior fossil fuel emission uncertainty.

For the “other” sector (**Error! Reference source not found.**) the uncertainty reductions in weekly emission rates are larger than that of the electricity generation sector. With one satellite (experiment 1) the posterior uncertainties in weekly emission rates from the other sector are already smaller than the actual national emissions from this sector, i.e., one satellite can provide informative estimates of weekly emission rates from the other sector with relative uncertainty below 100%. As previously explained, most of the observation information in this case goes toward constraining emissions from the other sector because the other sector has larger prior uncertainties than the electricity generation sector. When the prior uncertainties in the electricity generation sector were inflated by a factor of 10 (experiment 4), the posterior

uncertainties in emission rates for the other sector became larger than the actual emission rates for Germany, Poland and Australia, of comparable value for Brazil, and still smaller than the actual emission rates for China. Hence, if the prior uncertainty in the electricity generation and other sectors are of comparable magnitude, our results suggest that one satellite is able to constrain weekly emission rates from larger countries with large emissions like China.
Because the posterior uncertainties for the other sector show a stronger sensitivity to observations, it is useful to compare these posterior uncertainties to assess how different assumptions on observational uncertainties affect the results. Experiment 2 is similar to the default experiment (experiment 1) but with the addition of correlated systematic errors in the satellite observations (see Section **Error! Reference source not found.**). These correlated errors degrade the performance and increase the posterior uncertainty compared with the default experiment considerably, as they reduce the weight of the observations. Similarly, experiment 3 is the same as the default experiment except for the inclusion of representation error due to the mismatch in resolution between the satellite images and the atmospheric transport model (see Section **Error! Reference source not found.**). In this case representation error increases posterior uncertainties for the other sector by 17.8% in Australia, 36.3 and 40.3% in China and Germany, and about 63% in Australia and Poland relative to the default experiment. Nevertheless, one satellite with representation error still achieves substantial uncertainty reductions compared with a network of surface stations alone. We note that representation errors will furthermore be decreased when the resolution of the transport model is increased. Increasing the number of satellites from one to four (experiment 6) reduces posterior uncertainties by about 13–31% relative to the posterior uncertainties in the default experiment with one satellite (experiment 1). As for the electricity generation sector, experiment 5 shows a synergistic exploitation of bottom-up inventory information and top-down constraints by one satellite, which results in posterior uncertainties relative to the national emissions less than 11% for Brazil, China and Poland and less than 4% for Australia and Germany.

The inclusion of surface observations (experiment 7) does not result in substantial uncertainty reductions for emissions from the other sector compared with the default experiment with one satellite. This could be due to low sensitivity of the in situ observations to the fossil fuel emissions for the target countries. Experiment 8 shows that the 15 observational sites alone do not provide much constraint on the emissions from the other sector during the week of the experiment except for Germany and Poland, likely because of the far distance between the other target countries and the sites and the relatively short one-week assimilation window. This is confirmed in experiment 9 with the same 15 surface stations but half of the observational uncertainty, which further reduces posterior uncertainties in Germany and Poland but has a minimal impact on posterior uncertainties in the other three countries. Expanding the surface network to 141 sites (experiment 11) substantially reduces posterior uncertainties in emission rates from the other sector, especially in China. However, the posterior uncertainties are still much larger than for the experiment with one satellite. Similarly, adding radiocarbon observations to the 15 observational sites does not help much to constrain emissions for these target countries because of the long distance between the emissions and observational points and short assimilation window. With 141 observational sites the radiocarbon observations help to further constrain emission rates from the other sector. Although these experiments show that the surface network generally provides a poor constraint on fossil fuel emissions, it is important to remember that the constraint could be stronger with a longer assimilation window, and that the surface network is still important to observe background conditions and validate satellite measurements.

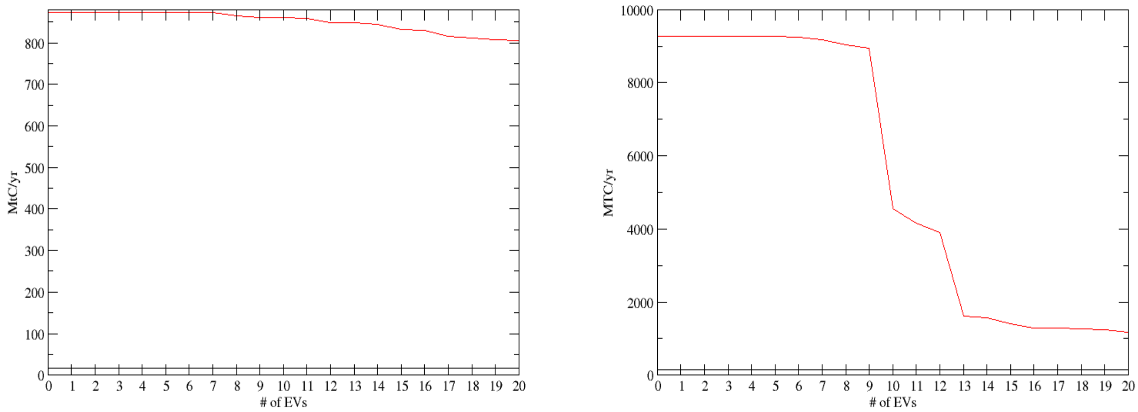

Figure 12: CCFFDAS posterior uncertainties of national total emissions (other sector and first week of June) from full Jacobian (black) and leading Eigenvalue approximation (red); left for Brazil and right for China.

As mentioned in Section 2.1, the monitoring of fossil fuel CO_2 emissions has to come with a sufficiently low uncertainty in order to be useful for policymakers. An advantage of the present CCFFDAS setup is that is uses the full Jacobians to derive the posterior uncertainties. In an ensemble-based approach the Jacobians would be represented by ensemble simulations. Such an ensemble must be of a sufficient size to properly represent the full PDFs, otherwise it could suffer from sampling errors. To examine how undersampling would affect the posterior uncertainties, we conducted an experiment where an approximation of the Jacobian was used in place of the full Jacobian. The approximate Jacobian was created using the leading Eigenvalues of the full Jacobian. Figure 12 shows the results for Brazil and China using the leading 1 to 20 Eigenvalues. Compared with using the full Jacobian, the posterior uncertainties using the approximate Jacobian are substantially higher, even if it captures the leading 20 Eigenvalues: >800 MtC/yr instead of 16 MtC/yr for Brazil, and >1100 MtC/yr instead of 133 MtC/yr for China. It is therefore essential for ensemble-based methods to use a sufficiently large ensemble size combined with ensemble methods such as covariance localisation to adequately represent the full PDFs. The present CCFFDAS setup can be used to support the setup of a suitable ensemble-based approach for quantification of posterior uncertainty.

Figure 13 shows the correlation in posterior uncertainties between different targets. The correlations between targets are generally negligible except for the negative correlations between the electricity generation and other sectors within the same country, which indicate that the sum over the sectors is better constrained than the difference between the sectors. For example, an underestimated emission rate for the electricity generation sector for one country would likely lead to an overestimated emission rate for the ‘other’ sector for the same country, and vice versa. There are also some small positive correlations, especially between the other sectors of a few countries. Such positive correlations are indicative of interconnections between the targets introduced by the control vector and modelling components. For example, some of these countries such as Germany and Poland share common PFTs, which are assumed to be controlled by global parameters. This creates a positive uncertainty correlation in natural fluxes over e.g. Germany and Poland, which translates to a positive uncertainty correlation for fossil fuel emissions between the two countries, especially for the other sector which tends to have more spread out emissions over the countries. By evaluating not only the posterior uncertainties but also the correlation between uncertainties, we can gain a more complete understanding of the constraints provided by different observations on the fossil fuel emissions.

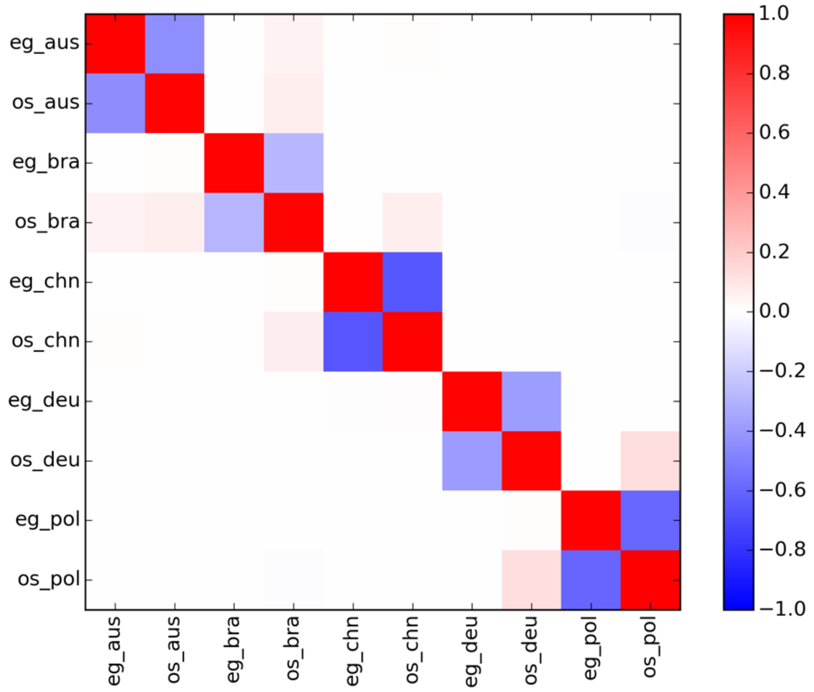

Figure 13: Posterior uncertainty correlation for default experiment (exp. 1 in Table 4).

The results presented so far (Tables 5 and 6) provide uncertainties $\sigma(y)$ for the emission rates in the first week of June 2008 in the unit MtC/yr. To extrapolate these uncertainties to annual emissions, we assume that we would obtain equal uncertainties for emissions in each of the other weeks in 2008 and that these uncertainties would be uncorrelated, which means that we can calculate the uncertainty in the annual emissions $\sigma(f_a)$ from the uncertainties in the weekly emissions $\sigma(f_1)$, …, $\sigma(f_{52})$ by

$$\sigma(f_a)^2 = \sum_{i=1}^{52} \sigma(f_i)^2 = \sum_{i=1}^{52} (\frac{\sigma(y)}{52})^2 = \frac{1}{52}\sigma(y)^2 \quad (16)$$

Tables 7 and 8 show the result of this calculation for the default experiment and the other sector (Table 7) and aggregated over both sectors (Table 8) compared to the respective national totals from the inventories as derived in Section 6.1. For the other sector, the posterior uncertainty would be similar to the uncertainty in the national total for Australia and Poland, a bit higher for Germany, and considerably lower for Brazil and China. For the total emissions (i.e. aggregated over both sectors) the posterior uncertainties are yet lower, both absolutely and in relation to the uncertainty in the national totals, with negative uncertainty correlations among the sectors in any given country. As mentioned this negative uncertainty correlation means that the sum over the sectors is better constrained than a single sector. Thus, as expected, relative to the inventories, CCFFDAS performs better for aggregated totals, in particular for countries with high negative correlations in sectorial uncertainties (Australia and China). The assumption of uncorrelated weekly uncertainties is certainly optimistic. The last row in Tables 7 and 8 explores the effect of uncertainty correlation in the annual uncertainty assuming that the weekly uncertainties are completely correlated throughout the year (e.g., an underestimated emission rate week 1 would lead to the same underestimation weeks 2 through 52). We note that completely correlated uncertainty is an extreme and unrealistic case, which ignores the information content added by each week of XCO2 observations. Also, the fact that an observation in a given week will act as a constraint on emissions in the same week but also on emissions in the weeks before will produce negative uncertainty correlations in the temporal domain, which tend to reduce the uncertainty in the annual integral. Hence, the truth lies somewhere between these two cases. We stress again that these approximate posterior uncertainties do not include the national totals from inventories, even though (as shown above) this is technically possible. Table 7 and 8 summarise the annual results for the two sectors.

Table 7: Uncertainty in annual emissions rates in MtC/yr; 'other' sector.

Description	Australia	Brazil	China	Germany	Poland
National total	1.8	9.3	128.6	4.2	2.8
Uncorrelated weekly emissions	2.2	3.0	24.8	7.0	2.7
Fully correlated weekly emissions	15.7	21.8	179.6	50.6	19.7

Table 8: Uncertainty in annual emission rates in MtC/yr; electricity generation sector.

Description	Australia	Brazil	China	Germany	Poland
National total	2.7	9.9	187.2	5.5	4.1
Uncorrelated weekly emissions	2.2	2.9	18.6	6.5	2.2
Fully correlated weekly emissions	115.8	21.1	134.3	46.8	15.8

9 Conclusion

This deliverable report provides a description of the CCFFDAS modelling framework, the applied QND methodology as well as the results obtained from the work performed in task 3.5 ‘Perform QND experiments with an advanced data assimilation system (CCFFDAS) to establish inversion strategy’. We have developed a prototype of a global Carbon Cycle Fossil Fuel Data Assimilation System (CCFFDAS) that combines the functionalities of the Fossil Fuel Data Assimilation System by Asefi-Najafabady et al. (2014) and of the Carbon Cycle Data Assimilation System by Kaminski et al. (2017a). The CCFFDAS was applied to assess a number of design aspects of the upcoming Monitoring and Verification Support capacity as part of the Copernicus CO_2 Monitoring mission (CO2M). The assessment was based on the Quantitative Network Design technique and quantified the mission's performance in terms of the posterior uncertainty in the totals of the sectorial fossil CO_2 emission rates for selected countries and the first week in June 2008. We analysed two different observing networks, ground based in situ observations and satellite based total column observations, in a range of configurations.

We find that

- At country scale, a single CO2M satellite achieves posterior uncertainties in the weekly sectorial emission rates well below the weekly emission rate for the national total for the sectors, assuming that annual emissions are evenly divided between all weeks.
- For each sector, a constellation of four satellites achieves a larger reduction in posterior uncertainty, i.e. the number of satellites matters. This added value of the extra satellites is more pronounced for the other sector than the electricity generation sector, where the uncertainty over China is reduced by about 30% for this particular case (first week in June 2008) when going from a single satellite to the four-satellite constellation. This is below the theoretical possible 50% reduction due to the different satellite tracks and with it differences in cloud cover and systematic errors for this particular week.
- Correlated systematic errors in the satellite XCO2 can seriously degrade the performance, resulting in increased posterior uncertainties from 15% to almost 130% relative to the case with no systematic errors.
- The representation error due to the mismatch in resolution between the satellite images and the atmospheric transport model increases posterior uncertainties, however, these uncertainties will be decreased when the resolution of the transport model is increased.
- If national inventories at weekly time scale were available, their inclusion would result in a strong reduction in posterior uncertainty (the largest reduction we obtained from all our experiments) compared with using atmospheric observations only, which quantifies the synergy / complementarity between the atmospheric (and other) observations and the inventories. The synergistic exploitation of diverse data steams is a particular strength of the CCFFDAS approach. However, by including national inventory data in the assimilation the obtained results are not an independent estimation of the emissions from atmospheric data anymore.
- A hypothetical projection of the posterior uncertainties in the weekly emission rate to the annual scale shows the potential for a CCFFDAS / CO2M verification mode (operating independently from the inventories), which may provide useful information that is complementary to the inventories with uncertainty ranges in the same order of magnitude.
- The inclusion of surface observations does not result in substantial uncertainty reductions for sectorial emissions compared with the default experiment with one satellite. However, we note that the current in situ network was not designed for observing anthropogenic emissions, nevertheless it is important to observe background conditions and validate satellite measurements.

- Adding radiocarbon observations helps to further constrain emission rates from the other sector especially for countries with a larger proportion of biogenic fluxes such as e.g. Brazil and Poland.

10 References

Agustí-Panareda, A., Diamantakis, M., Massart, S., Chevallier, F. and Munoz-Sabater, J., Barré, J., Curcoll, R., Engelen, R., Langerock, B., Law, R., Loh, Z., Morguí, J. A., Parrington, M., Peuch, V.-H., Ramonet, M., Roehl, C., Vermeulen, A. T., Warneke, T., and Wunch, D.: Modelling CO_2 weather - why horizontal resolution matters, Atmospheric Chemistry and Physics, 19, 7347-7376, doi: 10.5194/acp-19-7347-2019, 2019.

Asefi-Najafabady, S., Rayner, P. J., Gurney, K. R., McRobert, A., Song, Y., Coltin, K., Huang, J., Elvidge, C. and Baugh, K.: A multiyear, global gridded fossil fuel CO_2 emission data product: Evaluation and analysis of results, Journal of Geophysical Research: Atmospheres, 119(17), 10,213-10,231, doi:10.1002/2013JD021296, 2014.

Bhaduri, B., Bright, E., Coleman, P., and Urban, M.: LandScan USA: A high resolution geospatial and temporal modeling approach for population distribution and dynamics, GeoJournal, 69, 103-117, 2007.

Buchwitz, M., Reuter, M., Bovensmann, H., Pillai, D., Heymann, J., Schneising, O., Rozanov, V., Krings, T., Burrows, J. P., Boesch, H., Gerbig, C., Meijer, Y., and Löscher, A.: Carbon Monitoring Satellite (CarbonSat): assessment of atmospheric CO_2 and CH_4 retrieval errors by error parameterization, Atmospheric Measurement Techniques, 6, 3477-3500, doi: 10.5194/amt-6-3477-2013, 2013.

Broquet, G., Bréon, F.-M., Renault, E., Buchwitz, M., Reuter, M., Bovensmann, H., Chevallier, F., Wu, L. and Ciais, P.: The potential of satellite spectro-imagery for monitoring CO_2 emissions from large cities, Atmospheric Measurement Techniques, 11(2), 681–708, doi:10.5194/amt-11-681-2018, 2018.

Friedl, M., Strahler, A., and Hodges, J.: ISLSCP II MODIS (Collection 4) IGBP Land Cover, 2000-2001, doi:10.3334/ORNLDAAC/968, 2010.

Harris, I., Jones, P., Osborn, T., and Lister, D.: Updated high-resolution grids of monthly climatic observations - the CRU TS3.10 Dataset, International Journal of Climatology, 34, 623-642, doi: 10.1002/joc.3711, 2014.

Hascoët, L. and Pascual, V.: The Tapenade Automatic Differentiation tool: Principles, Model, and Specification, ACM Transactions On Mathematical Software, 39, doi: 10.1145/2450153.2450158, 2013.

Heimann, M. and Körner, S.: The global atmospheric tracer model TM3, Tech. Rep. 5, Max-Planck-Institut für Biogeochemie, Jena, Germany, 2003.

IEA, International Energy Agency: CO2 emissions from fuel combustion, OECD/IEA, Paris, 1997, available at http://www.iea.org/, 2011.

Kalnay, E., Kanamitsu, M., Kistler, R., Collins, W., Deaven, D., et al.: The NCEP/NCAR 40-Year Reanalysis Project, Bulletin of the American Meteorological Society, 77, 437-471, 1996.

Kaminski, T. and Mathieu, P.-P.: Reviews and syntheses: Flying the satellite into your model: on the role of observation operators in constraining models of the Earth system and the carbon cycle, Biogeosciences, 14(9), 2343–2357, doi:10.5194/bg-14-2343-2017, 2017.

Kaminski, T. and Rayner, P. J.: Reviews and syntheses: guiding the evolution of the observing system for the carbon cycle through quantitative network design, Biogeosciences, 14(20), 4755–4766, doi:10.5194/bg-14-4755-2017, 2017.

Kaminski, T., Scholze, M., Voßbeck, M., Knorr, W., Buchwitz, M., and Reuter, M.: Constraining a terrestrial biosphere model with remotely sensed atmospheric carbon dioxide, Remote Sensing of Environment, pp. 109-124, doi: 10.1016/j.rse.2017.08.017, 2017a.

Kaminski, T., Pinty, B., Voßbeck, M., Lopatka, M., Gobron, N., and Robustelli, M.: Consistent retrieval of land surface radiation products from EO, including traceable uncertainty estimates, Biogeosciences, 14, 2527-2541, doi: 10.5194/bg-14-2527-2017, 2017b.

Kaminski, T., Knorr, W., Rayner, P. J. and Heimann, M.: Assimilating atmospheric data into a terrestrial biosphere model: A case study of the seasonal cycle, Global Biogeochemical Cycles, 16(4), 14-1-14–16, doi:10.1029/2001GB001463, 2002.

Kaminski, T., Rayner, P. J., Voßbeck, M., Scholze, M. and Koffi, E.: Observing the continental-scale carbon balance: assessment of sampling complementarity and redundancy in a terrestrial assimilation system by means of quantitative network design, Atmospheric Chemistry and Physics, 12(16), 7867–7879, doi:10.5194/acp-12-7867-2012, 2012.

Knorr, W.: Annual And Interannual CO_2 Exchanges Of The Terrestrial Biosphere: Process-Based Simulations And Uncertainties, Glob. Ecol. Biogeogr., 9, 225-252, 2000.

Knorr, W. and Heimann, M.: Impact of drought stress and other factors on seasonal land biosphere CO_2 exchange studied through an atmospheric tracer transport model, Tellus, Ser. B, 47, 471-489, 1995.

Mahadevan, P., Wofsy, S. C., Matross, D. M., Xiao, X., Dunn, A. L., Lin, J. C., Gerbig, C., Munger, J. W., Chow, V. Y. and Gottlieb, E. W.: A satellite-based biosphere parameterization for net ecosystem CO2 exchange: Vegetation Photosynthesis and Respiration Model (VPRM), Global Biogeochemical Cycles, 22(2), doi:10.1029/2006GB002735, 2008.

Marland, G.: Uncertainties in Accounting for CO_2 From Fossil Fuels, Journal of Industrial Ecology, 12, 136-139, https://doi.org/10.1111/j.1530-9290.2008.00014.x, 2008.

Nakicenovic, N.: Socio-economic driving forces of emissions scenarios, in The Global Carbon Cycle: Integrating Humans, Climate and the Natural World, edited by B. C. Field and M. R. Raupach, pp. 225–242, Island Press, Washington, DC, 2004.

Pinty, B., Lavergne, T., Voßbeck, M., Kaminski, T., Aussedat, O., Giering, R., Gobron, N., Taberner, M., Verstraete, M. M., and Widlowski, J.-L.: Retrieving surface parameters for climate models from MODIS-MISR albedo products, J. Geophys. Res., 112, doi: 10.1029/2006JD008105, 2007.

Pinty, B., Clerici, M., Andredakis, I., Kaminski, T., Taberner, M., Verstraete, M. M., Gobron, N., Plummer, S., and Widlowski, J.-L.: Exploiting the MODIS albedos with the Two-stream Inversion Package (JRC-TIP): 2. Fractions of transmitted and absorbed fluxes in the vegetation and soil layers, Journal of Geophysical Research - Atmospheres, 116, D09 106, doi: 10.1029/2010JD015373, 2011

Rayner, P., Michalak, A. M. and Chevallier, F.: Fundamentals of Data Assimilation, Geoscientific Model Development Discussions, 1–21, doi:10.5194/gmd-2016-148, 2016.

Rödenbeck, C.: Estimating CO_2 sources and sinks from atmospheric mixing ratio measurements using a global inversion of atmospheric transport, Technical Report 6, Max Planck Institute for Biogeochemistry, Jena, Germany, 2005.

Tarantola, A.: Inverse Problem Theory and methods for model parameter estimation, SIAM, Philadelphia, 2005.

UNFCCC: United Nations Framework Convention on Climate Change, online, lastaccessed 10 December 2018, http://unfccc.int/files/essential_background/convention/background/application/pdf/convention_text_with_annexes_english_for_posting.pdf, 1992.

Vogel, F. R., Hammer, S., Steinhof, A., Kromer, B. and Levin, I.: Implication of weekly and diurnal 14C calibration on hourly estimates of CO-based fossil fuel CO2 at a moderately polluted site in southwestern Germany, Tellus B, 62(5), 512–520, doi:10.1111/j.1600-0889.2010.00477.x, 2010.

Ziskin, D., Baugh, K., Hsu, F. C., Ghosh, T., and Elvidge, C.: Methods used for the 2006 radiance lights, in: Proc. Asia-Paci_c Adv. Network, vol. 30, pp. 131-142, 2010.

Document History

Version	Author(s)	Date	Changes
0.1	Marko Scholze Hans Chen Thomas Kaminski Michael Vossbeck	21/09/2020	Initial version
1.0	Marko Scholze Hans Chen Thomas Kaminski Michael Vossbeck	26/10/2020	Revised version according to comments from internal reviewer

Internal Review History

Internal Reviewers	Date	Comments
SRON	11/10/2020	See commented version and review form

Estimated Effort Contribution per Partner

Partner	Effort
ULUND	1.0 PM
Total	**1.0 PM**